Research Paper

Long term trends of mesospheric ice layers: A model study

Franz-Josef Lübken [*], Gerd Baumgarten, Uwe Berger [†]

Leibniz-Institute of Atmospheric Physics, Schloss-Str. 6, 18225, Kühlungsborn, Germany

ARTICLE INFO

ABSTRACT

Trends derived from the Leibniz-Institute Middle Atmosphere Model (LIMA) and the MIMAS ice particle model (Mesospheric Ice Microphysics And tranSport model) are presented for a period of 138 years (1871–2008) and for middle, high, and arctic latitudes, namely 58°N, 69°N, and 78°N, respectively. We focus on the analysis of mesospheric ice layers (NLC, noctilucent clouds) in the main summer season (July) and on yearly mean values. Model runs with and without an increase of carbon dioxide and water vapor (from methane oxidation) concentrations are performed. Trends are most prominent after ~1960 when the increase of both CO_2 and H_2O accelerates. It is important to distinguish between tendencies on geometric altitudes and on given pressure levels converted to altitudes ('pressure altitudes'). Negative trends of (geometric) NLC altitudes are primarily due to cooling below NLC altitudes caused by CO_2 increase. Increases of ice particle radii and NLC brightness with time are mainly caused by an enhancement of water vapor. Several ice layer and background parameter trends are similar at high and arctic latitudes but are substantially different at middle latitudes. This concerns, for example, occurrence rates, ice water content (IWC), and number of ice particles in a column. Considering the time period after 1960, geometric altitudes of NLC decrease by approximately 260 m per decade, and brightness increases by roughly 50% (1960–2008), independent of latitude. NLC altitudes decrease by approximately 15–20 m per increase of CO_2 by 1 ppmv. The number of ice particles in a column and also at the altitude of maximum backscatter is nearly constant with time. At all latitudes, yearly mean NLC appear at altitudes where temperatures are close to 145±1 K. Ice particles are present nearly all the time at high and arctic latitudes, but are much less common at middle latitudes. Ice water content and maximum backscatter (β_{max}) are highly correlated, where the slope depends on latitude. This allows to combine data sets from satellites and lidars. Furthermore, IWC and the concentration of water vapor at β_{max} are also strongly correlated. Nearly all trends depend on a lower limit applied for β_{max}, e.g., IWC and occurrence rates. Results from LIMA/MIMAS are in very good agreement with observations.

1. Introduction

Noctilucent clouds (NLC) consist of ice particles which are present in the summer mesopause region at middle and polar latitudes. They reflect the very low background temperatures present under these conditions. At mid-latitudes NLC are observed from the ground by naked eye (see review in Gadsden and Schröder, 1989). Modern lidar technology allows to measure the morphology of NLC in great detail (see, for example, Hansen et al., 1989; von Zahn et al., 1998; Gerrard et al., 1998; von Cossart et al., 1999; Chu et al., 2003; Collins et al., 2009; Gerding et al., 2013; Fiedler et al., 2017, and references therein). These clouds are also known as polar mesosphere clouds (PMC). Instruments on various satellites have been used to detect PMC and to investigate

potential trends (see, e.g., Olivero and Thomas, 1986; Thomas et al., 1989; Shettle et al., 2002; DeLand and Thomas, 2015; Russell et al., 2015; Hervig et al., 2016a). In this paper we use the term NLC for all ice layers, even if they are not observable by naked eye or by lidar. The question whether or not NLC/PMC are potential indicators for long term changes in the middle atmosphere caused by anthropogenic activities is controversially discussed in the literature (Thomas, 1996; Thomas et al., 2003; von Zahn, 2003). We have developed a model of ice particle nucleation, growth, sedimentation, and sublimation where millions of dust particles are released and traced in the summer mesopause region where they eventually create ice (Berger and von Zahn, 2002; von Zahn and Berger, 2003; Lübken et al., 2009; Berger and Lübken, 2015).

In the past we focussed on middle latitudes and on the period after

---

1961. More recently, we have extended our simulation to a longer period, namely 1871 to 2008, and introduced increases of CO_2 and CH_4 (see Lübken et al., 2018, hereafter referred to as LBB18). The analysis presented in this paper is based on the same simulations as in LBB18. The purpose of the current paper is to extend LBB18 with respect to the following topics: i) to study the morphology and reasons for NLC trends in more detail, ii) to extend the trend analysis to high/arctic latitudes, and iii) to compare with observations.

In the next sections we introduce the models and present some results from temperature trends at NLC altitudes. Trends in ice layer parameters are described in section 4. Some selected correlations and comparisons with observations are discussed in sections 5 and 6, respectively.

2. Model setup

We provide an overview of those model aspects which are important for this paper. More detailed descriptions are available in the literature (Berger and von Zahn, 2002; Berger, 2008; Berger and Lübken, 2011, LBB18). The model consists of two main components, namely LIMA (Leibniz-Institute Middle Atmosphere Model) and MIMAS (Mesospheric Ice Microphysics And tranSport model). In MIMAS a total of 40 million dust/ice particles drift in the atmosphere according to three-dimensional and time-dependent background winds, eddy diffusion, and sedimentation. Eventually, ice particles are formed and grow in regions of supersaturation (S>1, S = degree of saturation). They finally sublimate when regions of S<1 are encountered, mainly around 83–84 km. This process leads to a redistribution of water vapor, namely a reduction at mesopause altitudes (and a few km below), and an enhancement at NLC altitudes. This effect is commonly called 'freeze drying' (see Fig. 5 in Lübken et al., 2009).

LIMA is nudged to reanalysis data in the lower atmosphere. In former studies we have concentrated on the time period after 1961 because data from ERA-40 were available from then on. In LBB18 we extended trend studies to the period 1871–2008 (138 years) since the 20th century reanalysis data from NOAA-CIRES became available (Compo et al., 2011). The effect of gravity waves are taken into account in LIMA by parametrization according to Medvedev and Klaassen (2000). In the model runs performed for this paper we have taken background wind conditions and gravity wave forcing from a representative year (1982) which is then used for all years (see discussion in section 7). In other words, the dynamical forcing of the mesopause region is identical for all years in LIMA. The dynamical and compositorial conditions in LIMA are forwarded to MIMAS as is sketched in Fig. 1. For water vapor the effects of freeze drying, photolysis etc. are separately taken into account in MIMAS. The long term increase of CO_2 concentration is considered according to observations in the troposphere. For CO_2 we use the time series measured at Mauna Loa (19°N, 155°W) and historical CO_2 records (see Etheridge et al., 1998, and the ftp site given in the acknowledgements). Furthermore, an increase of water vapor in the mesosphere is

introduced taking into account the increase of methane in the troposphere and transport from below (the latter is assumed to be constant). Note that methane is nearly completely converted to water vapor in the mesosphere by photochemical processes (see LBB18 for more details). We have performed three runs, namely A: increase of CO_2 and H_2O, B: increase of CO_2, H_2O is kept constant, and C: increase of H_2O, CO_2 is kept constant. We will occasionally use the following symbols in this paper to remind about these scenarios: for run A: $CO_2\uparrow, H_2O\uparrow$, for run B: $CO_2\uparrow$, $H_2O\leftrightarrow$, and for run C: $CO_2\leftrightarrow, H_2O\uparrow$.

MIMAS determines the positions and radii of 40 million ice particles, i. e., 2.7×10^{14} data points from MIMAS are compressed into the yearly mean values shown later (40 million particles $\times$ 3 coordinates $\times$ 2 radii (dust, ice) $\times$ 138 years $\times$ 31 days/year (1.7.–31.7.) $\times$ 86,400 s/day, divided by the time resolution of Δt=300 s). This information is used to calculate ice layer parameters in a given latitude/longitude bin and
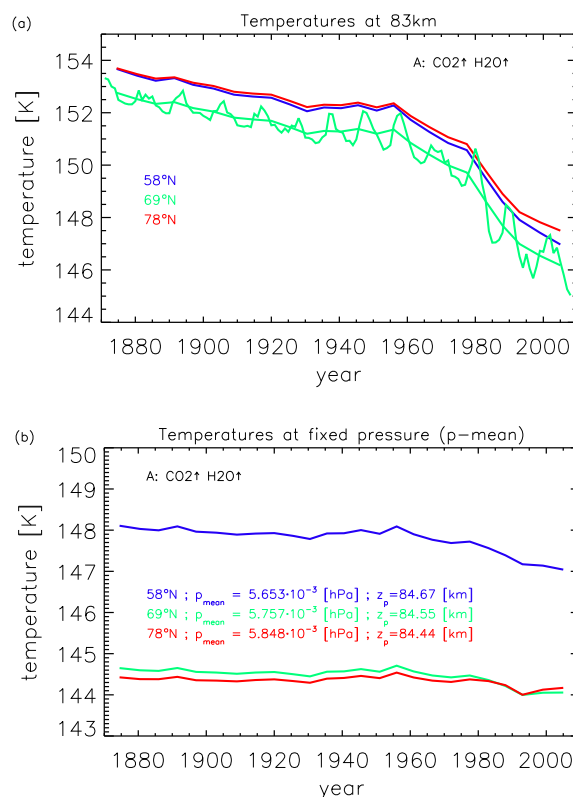

Fig. 2. (a) Temperatures at a fixed geometric altitude (83 km) for run A. Data for 69°N are shown with and without smoothing over a solar cycle. (b) Temperatures at a fixed pressure level p_{mean} defined in the text. Colors indicate different latitudes (see insert).
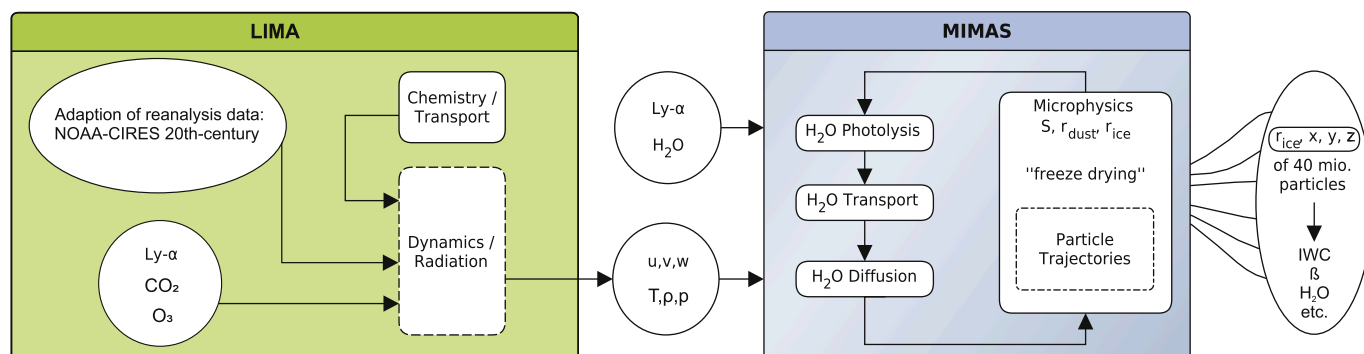

Fig. 1. Scetch of the LIMA (green) and MIMAS (blue) models. See text for more details.

within a given time period (see example shown in Fig. 2 in LBB18). The position of each dust/ice particle in MIMAS is known to an accuracy of few meters. After averaging, the effective vertical resolution of MIMAS is 100 m. The horizontal resolution of the output of MIMAS used for further analysis is 120 longitude bins (0–360) and 53 latitude bins (1° each from 38°N to 90°N). We concentrate on 3 latitude ranges, namely 58±3°N, 69±3°N, and 78±3°N which are labeled 'middle', 'high' and 'arctic' latitudes in this paper. Apart from background conditions we concentrate on mean ice particle radii (r_{ice} in units of nm), the maximum backscatter coefficient at a wavelength of 532 nm (β_{max} in units of 10^{-10}/(m·sr)), the amount of ice in a column ('ice water content', IWC, in units of g/km^2), and the number of ice particles in a column (N_{ice} in units of 1/cm^2). The backscatter coefficient β gives the cross section per unit volume and per unit solid angle for photons being scattered in the backward direction. For backscattering from NLC particles β is frequently determined by comparing with backscattering from molecules (see, for example, Baumgarten et al., 2002). In this paper we consider the maximum backscatter from NLC particles (β_{max}), namely the backscatter coefficient at the peak of the NLC layer (see Fig. 1 in LBB18).

We consider the center of the summer season only, i. e., July. Whenever an ice layer occurs in a given latitude/longitude bin and time segment in MIMAS, we call this an 'event' and extract from MIMAS mean ice layer and background parameters, for example, β_{max}, the altitude of β_{max}, IWC, temperature, pressure, and water vapor concentration. The maximum number of events per year is N_{max} = 89,280 given by the number of latitudes within each range (6), longitudes (120), days (31), and time slots per day (4). Occurrence rates are determined in each latitude band by dividing the number of events by N_{max}. Since some observations detect NLC only above a certain threshold we have introduced a lower limit β_{lim} when determining, for example, occurrence rates or mean NLC altitudes. In other words, only NLC above a given threshold ($\beta_{max} > \beta_{lim}$) are considered when averaging. The special case β_{lim}=0 means that all events are taken into account, even those where β_{max} is very small.

In order to describe the development of the mean background atmosphere at NLC altitudes we show, for example, temperatures at each latitude range and for each year but at a pressure being located close to NLC altitudes which is then used for all 138 years (p_{mean}). The equivalent pressure altitude, z_p, is given by z_p=H·ln(p_0/p_{mean}) with p_0=1013 hPa and H=7000 m.

As is well known, temperatures in the entire middle atmosphere decrease with time mainly due to enhanced cooling by CO_2 (e.g., Roble and Dickinson, 1989; Garcia et al., 2007; Berger and Lübken, 2011; Marsh et al., 2013; Lübken et al., 2013). At NLC altitudes this cooling leads to an altitude decrease of pressure levels. This is commonly referred to as the 'shrinking effect' and is highly relevant in this study. For example, the temporal development of NLC altitudes is significantly larger when considering geometric altitudes instead of pressure altitudes (i. e., pressure levels converted to altitudes as described above).

3. Temperature trends in the NLC region

In Fig. 2a temperatures at a fixed geometric altitude of 83 km are shown for all 138 years. We have compared temperature trends from an earlier version of LIMA with the global circulation model WACCM (Whole Atmosphere Community Model) but for a shorter time period and find good agreement (Garcia et al., 2007; Lübken et al., 2013). Temperatures are rather similar at all three latitudes, i. e., the difference is less than 1 K. Interestingly, temperatures at 69°N are slightly lower compared to higher latitudes, which is a consequence of different pressure levels involved (see below). Note that the decrease of temperatures in Fig. 2a is systematically stronger after ~1960 compared to before. This gradient change is observed in most parameters shown in this paper. We therefore occasionally divide the analysis of slopes into two periods, namely before and after 1960. We have listed some important slopes for the period after 1960 in Table 1. The temperature

Table 1
Rate of change with time after 1960 in (units)/decade.

latitude	run	β_{lim}	slope
temperature in 83 km			[K/dec]
58	A	0.0	−1.176
69	A	0.0	−1.172
78	A	0.0	−1.102
temperature at p_{mean}			[K/dec]
58	A	0.0	−0.205
69	A	0.0	−0.135
78	A	0.0	−0.074
β_{max}			10^{-10}/(m·sr)/dec
58	A	1.0	0.108
69	A	1.0	0.213
78	A	1.0	0.177
ice radius @ β_{max}			[nm/dec]
58	A	0.0	0.494
69	A	0.0	0.753
78	A	0.0	0.649
height of β_{max}			[m/dec]
58	A	1.0	−232.
69	A	1.0	−269.
78	A	1.0	−268.
ice water content			[g/km^2/dec]
58	A	0.0	0.807
69	A	0.0	2.244
78	A	0.0	1.953
occurrence rate			[%/dec]
58	A	0.0	3.479
69	A	0.0	1.347
78	A	0.0	1.054

change is on the order of −1.7 K in the period 1871 to 1960, and larger thereafter, namely roughly −5 K for the period 1960 to 2008. This is mainly due to the shrinking effect explained in section 2. In Fig. 2a we show two lines for 69°N, namely one with full resolution (i. e., one data point per year), and another one smoothed over half a solar cycle. As can be seen, solar activity causes some modulation of temperatures, which is basically true for all parameters shown in this paper. Since the impact of solar activity is not the subject of this paper we will only show time series smoothed over half a solar cycle in the following.

To demonstrate the effect of shrinking we show in Fig. 2b temperatures at a pressure level (p_{mean}) which is derived from mean NLC altitudes but is fixed for all 138 years. Since NLC altitudes are different for different latitudes and also for different runs, p_{mean} is also different for different latitudes/runs. For run A the pressure levels are p_{mean}=5.6526E-03 hPa, 5.7573E-03 hPa, and 5.8479E-03 hPa at 58°N, 69°N, and 78°N, respectively. The corresponding pressure altitudes are z_p=84.67 km, 84.55 km, and 84.44 km, respectively, i. e., very close to each other. As can be seen in Fig. 2b temperatures at p_{mean} are very similar at high and arctic latitudes, but are significantly larger (by ~3.5 K) at middle latitudes. This basically reflects the latitudinal gradient of temperatures at NLC altitudes (Lübken et al., 2013). The rate of temperature change on fixed pressure levels is small in all periods, even after 1960 (−0.06 K/dec to −0,2 K/dec). The total temperature drop over 138 years is also very small, namely less than ~1 K. We conclude that temperatures at a fixed pressure level close to the NLC layer are nearly constant over time. This is true for all latitudes and highlights the fact that temperature changes are small at NLC altitudes whereas significant cooling occurs at lower altitudes leading to a substantial shrinking and subsidence of pressure levels to lower geometric altitudes.

In Fig. 3a temperatures at β_{max} for β_{lim}=0.0 are shown. As can be seen temperatures at β_{max} are very similar at all latitudes (the deviation is less than ~0.5 K) when only regions with ice are considered. Temperatures increase slightly over time but are close to 145±1 K for all times and all latitudes. In other words, the maximum backscatter within an NLC appears (on average) close to 145±1 K, independent of time and latitude.

This is a consequence of the transition from super- to subsaturation ($S=1$) which primarily depends on temperature whereas water vapor is of secondary importance (see, e. g., Berger and von Zahn, 2002).

In Fig. 3a we also show frost point temperatures, T_{frost}, using water vapor mixing ratios at the altitude of β_{max}, which are somewhat enhanced compared to background conditions because of freeze drying. As can be seen, temperatures at β_{max} are lower by ~1 K compared to T_{frost}. This is due to the fact that particle temperatures in general are slightly higher compared to ambient temperatures (see, for example, Eidhammer and Havnes, 2001; Espy and Jutt, 2002; Rapp and Thomas, 2006), and that the Kelvin effect needs to be taken into account when calculating the degree of saturation (Berger and von Zahn, 2002).

If we take temperatures at the altitude of β_{max} in all latitude/longitude/time bins (including those where no NLC exist) temperatures at middle latitudes are considerably higher (blue dashed line in Fig. 3a). This implies that NLC at middle latitudes occur preferentially in regions where temperatures are lower compared to other locations in the same latitude band. This is consistent with lidar temperature measurements at 54°N during summer with and without NLC (Gerding et al., 2007). The temperature difference is negligible for 69°N and 78°N (not shown), i. e., temperatures in regions with NLC are approximately the same compared to regions without NLC.

A histogram of all temperatures at β_{max} is shown in Fig. 3b for an arbitrary year (1954) and $\beta_{lim}=0.$, i. e., all events are considered. The sums of all events in that year are 36,998, 77,024, and 81,746 (from a maximum of 89,280, see section 2) for 58°N, 69°N, and 78°N, respectively. The distribution is nearly of Gaussian shape and nearly symmetric around the mean. Mean temperatures and standard deviations are 144.0±2.8 K, 144.3±2.4 K, and 144.4±2.1 K, respectively. Mean temperatures at β_{max} at different latitude bands in a given year therefore
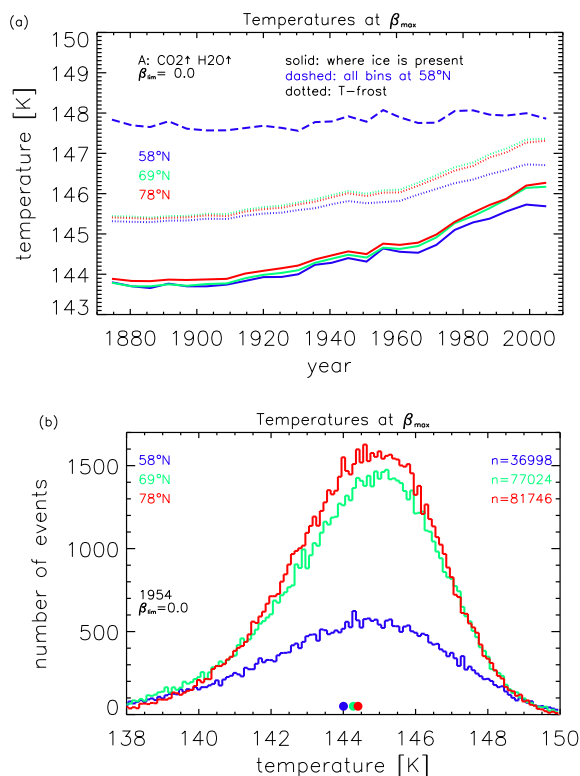
deviate by less 0.5 K. This is surprising when considering the complexity of ice particle formation and the variation of background conditions within the season and with latitudes. The standard deviations of the distributions shown in Fig. 3b are 2.80 K, 2.42 K, and 2.13 K at 58°N, 69°N, and 78°N, respectively. Several processes might have contributed to this variability, including tides. We will investigate the reason for the latitudinal variation of mean values and variations in more detail in the future. Fig. 3b also demonstrates the huge amount of information available from LIMA/MIMAS which is further condensed to the long term evolution of yearly mean values discussed in this paper.

Temperatures at β_{max} (Fig. 3a) increase slightly (by ~2 K in 138 years) mainly because the concentration of water vapor at β_{max} increases. This allows temperatures to be slightly higher in order to fulfill the $S=1$ condition. This can be seen in Fig. 4 where pressure values at β_{max} are shown. For run A these pressures increase with time by ~0.008 hPa at high and arctic latitudes and ~0.005 hPa at mid latitudes, respectively. Because of the negative temperature gradient at mesospheric altitudes, higher pressures correspond to lower altitudes and higher temperatures. The fact that freeze drying is the main reason for this effect can be seen when comparing with run B where H_2O is kept constant over time (dashed red line in Fig. 4). Subsequently, the increase of water vapor due to freeze drying is smaller, and the increase of pressures and temperatures at β_{max} is also smaller.

4. Trends of ice particle parameters

4.1. Maximum backscatter, ice particle radii, and number densities

The temporal development of β_{max} is shown in Fig. 5a, where a limit of $\beta_{lim}=1$ is applied in order to concentrate on NLC with considerable brightness. Note, that Fiedler et al. (2017) uses $\beta > 1$ to derive statistics for NLC from lidar observations. Yearly mean β_{max}-values are rather similar at all latitudes, although the distributions are rather different (Fig. 5b, we will come back to this distribution later). In case that both CO_2 and H_2O increase (run A) β_{max} increases by ~50% in total, where this increase occurs mainly after about 1960 and is slightly stronger at high and arctic (compared to middle) latitudes. If only CO_2 increases (run B, i. e., H_2O is constant) β_{max} is nearly constant and even slightly decreases at all latitudes. We summarize that the increase of β_{max} in run A is caused by an increase of water vapor and not by a decrease of temperatures. The fact that β_{max} is even slightly decreasing although it is getting colder (run B, Fig. 5a) is presumably related to the temperature dependence of microphysical processes involved. For example, at lower temperatures more ice particles are formed since the barrier for nucleation is lower (Kelvin effect). Indeed, the occurrence rate for run B increases with time (shown later). Obviously the creation of clouds with less brightness is favored. We note, that such a scenario is consistent with simultaneous observations of temperatures by falling spheres and
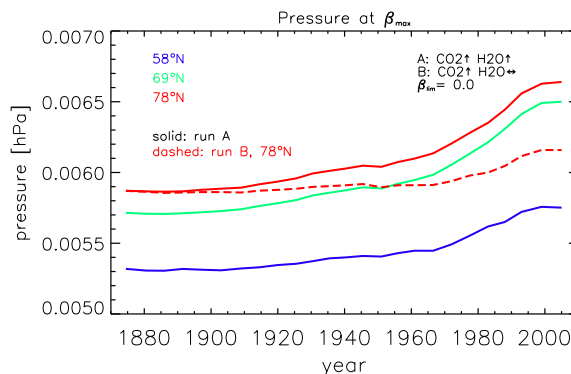

Fig. 3. (a) Temperatures at β_{max} for run A and $\beta_{lim}=0$. Solid: only where ice is present, dashed: in all bins (only for 58°N). Frost point temperatures are also shown (dotted lines) using water vapor concentrations at β_{max}. (b) Histogram of temperatures at β_{max} for an arbitrary year (1954) considering all events ($\beta_{lim}=0$). The total number of events at each latitude is given in the insert. The dots close to the x-axis represent mean values. Colors indicate different latitudes (see insert).

Fig. 4. Pressures at β_{max} for run A (solid) and run B (dashed, only for 78°N). Colors indicate different latitudes (see insert).
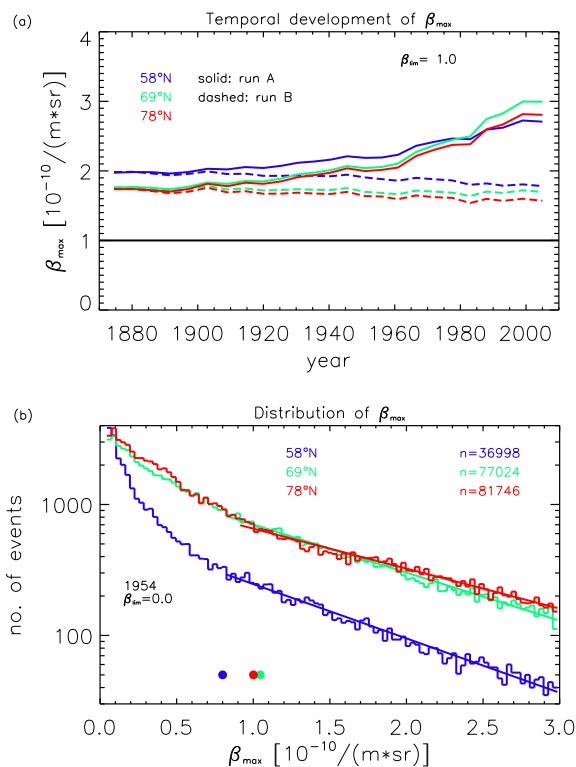
Fig. 5. (a) Temporal development of β_{max} for run A (solid lines) and run B (dashed lines) applying a threshold of $\beta_{lim} = 1$. Colors indicate different latitudes (see insert). (b) Histogram of β_{max}-values for an arbitrary year (1954). The total number of events is given in the insert. The dots close to the x-axis indicate mean values. The lines show a linear fit to the logarithm of numbers.

Fig. 6. (a) Number of ice particles in a column for run A (solid lines) and run C (dashed lines). Results for run B are very similar to run A. (b) Mean ice particle radii for run A (solid lines) and run B (dashed lines). Results for run C are very similar to run A. Colors indicate different latitudes (see insert).

NLC by lidar (Lübken et al., 1996, Fig. 9).

In Fig. 6a the number of ice particles in a column (N_{ice}) is shown. Generally speaking N_{ice} is nearly constant for all runs and at all latitudes (results for run B are not shown since they are nearly identical to run A). For runs A and B (i. e., when CO_2 is increasing) N_{ice} is slightly decreasing with time at high/arctic latitudes but only by 2–5%. Results for ice particle number densities (in units of $1/cm^3$) at altitudes of β_{max} are rather similar (not shown). As can be seen in Fig. 6b mean ice particle radii (r_{ice}) increase with time but virtually only if water vapor increases, i. e., for runs A and C (results for run C are not shown since they are very similar to run A). If H_2O is kept constant (run B) particle radii are practically constant in time. In summary, the increase of β_{max} in runs A and C is mainly due to an increase of particle radii caused by enhanced water vapor concentration, whereas the number of particles is basically constant. Fig. 6a also demonstrates that N_{ice} is significantly smaller at middle latitudes compared to high and arctic latitudes.

At the beginning of the time period, mean ice particle radii are rather similar at high and arctic latitudes, whereas they are slightly larger (by ~1–2 nm) at middle latitudes (Fig. 6b). The increase of radii with time is somewhat stronger at high and arctic latitudes, so that all three curves are rather similar at the end of the time period. For run A ($CO_2\uparrow$,$H_2O\uparrow$) particle radii (r_{ice}) increase over time by a total of roughly 4 nm in 138 years, i. e., by approximately 17%. The increase is basically negligible if water vapor is kept constant (run B). Note that it is not straight forward to convert a change of mean radii (e.g. increase by 17%) to a change of mean backscattering applying results from scattering theory ($\beta_{max} \sim r^{5.3}$). The strong sensitivity of β_{max} to radii requires a consideration of the entire distribution of radii for all events as shown in Fig. 5b. Even the distribution within each single event may be important.

The distributions in Fig. 5b show that the number of events is significantly larger at high/arctic latitudes (compared to mid-latitudes)
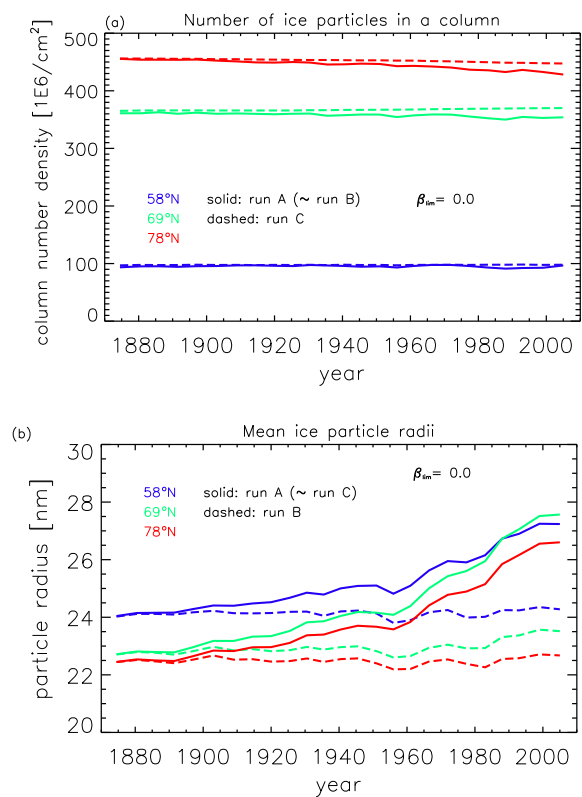
for all β_{max}-values, but the mean values are rather similar. This implies that the chance to observe, for example, bright NLC is larger at high/arctic latitudes, in agreement with lidar observations (Gerding et al., 2013; Fiedler et al., 2017). The distributions in Fig. 5b show an exponential decrease, except for very low β_{max}-values. Note that the relationship between a certain ice layer parameter (e.g. β_{max}) and another parameter (i. e., IWC) is in general highly non-linear. This implies that an exponential decrease of the distribution of β_{max} does not necessarily imply a similar behavior of other ice layer parameters (see Berger et al., 2019, for a detailed discussion on this topic).

4.2. NLC altitudes

In Fig. 7a geometric altitudes of β_{max}(z_{NLC}^{geo}) are shown as a function of time for all three latitudes and for runs A and C. As can be seen, these altitudes decrease substantially (and mainly after ~1960) but only if CO_2 increases (run A) whereas the decrease is much smaller if CO_2 is kept constant and only H_2O increases (run C). As mentioned above, the main reason for the strong decrease of z_{NLC}^{geo} is the shrinking effect due to cooling of the entire middle atmosphere below NLC heights. In case of run C, CO_2 is constant (no cooling) and shrinking is basically absent. On the other hand, H_2O increases over time which shifts the level of S=1 to higher temperatures, therefore to higher pressures and lower geometric altitudes. Therefore, z_{NLC}^{geo} is also decreasing for run C, but the decrease is much smaller compared to run A. More quantitatively, geometric altitudes of β_{max} decrease by ~1.5 km since 1871 (run A). The rate of change in recent decades (since ~1960) is roughly −260 m/dec (see Table 1). The altitude of β_{max} varies comparatively little with latitude. It is ~200–400 m higher at 69°N (compared to 58°N), and again higher by approximately the same amount when comparing 69°N and 78°N. The difference in NLC altitudes gets even smaller with time. The similarity of

NLC altitudes at all latitudes is a consequence of the fact that temperatures at these heights are nearly independent of latitude (see Fig. 2 in Lübken et al., 2013).

In Fig. 7b we show a comparison of altitudes of β_{max} from LIMA/MIMAS and measurements of NLC by the Rayleigh-Mie-Raman (RMR) lidar at ALOMAR (Arctic Lidar Observatory for Middle Atmosphere Research, 69°N) where a limit of $\beta_{lim}=4$ has been applied in both cases (Fiedler et al., 2017). Note that we use LIMA/MIMAS data for each year in this plot, i. e., we have not averaged over half a solar cycle. Lidar observations of NLC are available since 1997 which offers the opportunity to compare with LIMA/MIMAS. Typical errors of mean lidar altitudes are ±40–80 m, whereas standard deviations are significantly larger (±1.1–1.5 km). As can be seen in Fig. 7b the agreement between model and observations is excellent as far as mean NLC altitudes are concerned. If we use data from 1997 to 2008 only we arrive at slopes of −206±53 m/dec and −198±50 m/dec for ALOMAR and LIMA/MIMAS, respectively, again in excellent agreement. Note that a significant part of this trend is given by the impact of solar cycle. We hesitate to extend the comparison beyond 2008 since the development of ozone also plays a role on such short time periods and LIMA/MIMAS runs beyond 2008 are currently not available (see Lübken et al., 2013, for a discussion of stratospheric ozone changes and mesospheric temperatures). We have performed a similar comparison with the RMR lidar measurements at Kühlungsborn (54°N, not shown) (Gerding et al., 2013). Again, the agreement is very good but the natural variability is even larger (less NLC occurrence) which makes an experimental detection of altitude trends even more difficult.

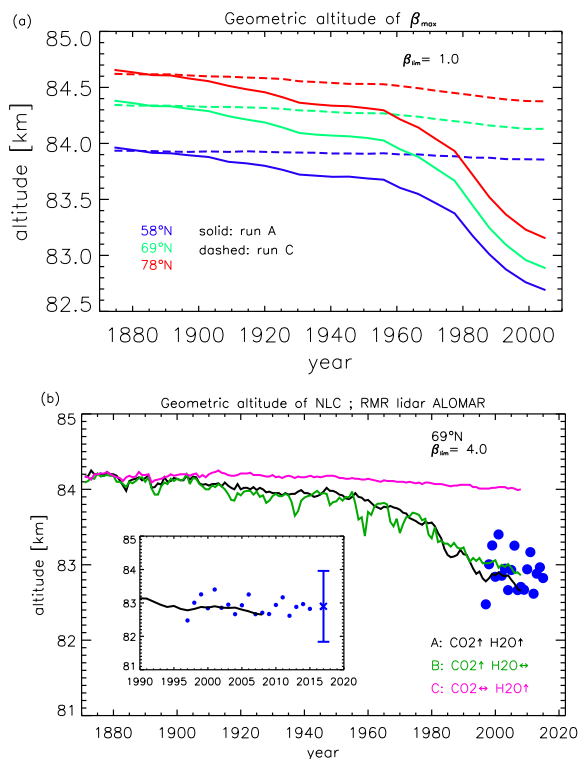In Fig. 7a we have applied a limit of $\beta_{lim}=1$ in order to consider NLC

of considerable strength only. Since z_{NLC}^{geo} depends on this limit we show in Fig. 8 the shift of z_{NLC}^{geo} as a function of β_{lim} with respect to the case where $\beta_{lim}=0$. Altitude shifts are shown for all three latitudes and for two years (1920, 1980) which are representative for the period before and after 1960, respectively. For example, at 69°N the geometric altitude of β_{max} decreases by ~300–400 m when a limit of $\beta_{lim}=2$–4 is chosen (relativ to $\beta_{lim}=0$). This is consistent with lidar observations at ALOMAR which show stronger NLC at lower altitudes (Fiedler et al., 2017). As can be seen in Fig. 8 altitude shifts are rather independent of time but are considerably higher at middle latitudes compared to high/arctic latitudes, in agreement with lidar measurements (Gerding et al., 2013; Fiedler et al., 2017).

4.3. Ice water content and occurrence rates

The amount of water bound in ice particles in a column (IWC) is shown in Fig. 9a. The IWC is rather similar at high/arctic latitudes but is much smaller at middle latitudes. This is a consequence of larger ice radii and higher ice number densities at high/arctic latitudes (see Fig. 6a and 6b). As expected, IWC depends strongly on β_{lim} (compare lines for $\beta_{lim}=0$ and 1 in Fig. 9a). This is due to the fact that when switching from $\beta_{lim}=1$ to $\beta_{lim}=0$ some events with small β-values (between 0 and 1) and small IWC are added (see Fig. 5b) which reduces the mean IWC value. IWC results from SOFIE and SBUV are in the range of approximately 40–110 g/km^2, depending on latitude (Hervig et al., 2015, 2016b; 2016a). Considering LIMA/MIMAS results for $\beta_{lim}=1$ (Fig. 9a), mean IWC values at the end of the time period and in the latitude band around 69°N and 78°N are approximately 65–70 g/km^2. The dependence of IWC on the choice of β_{lim} is highlighted further in Fig. 9b. As can be seen, IWC from LIMA/MIMAS for 69°N and 78°N and $\beta_{lim}>1$ achieve values between roughly 60 g/km^2 and 100 g/km^2, i. e. in the range observed by SOFIE and SBUV. Note that it is not straight forward to convert the sensitivities of SBUV or SOFIE to equivalent β_{lim}-values.

As can be seen in Fig. 10a occurrence rates are rather different at high/artic latitudes compared to middle latitudes. Results are shown for $\beta_{lim}=0$ (solid lines), i. e., even tiny ice layers are considered. Occurrence rates are determined by comparing all latitude/longitude/time bins where ice is present to the total number of bins in the latitude range under consideration, $N_{max}=89280$ (see section 2). These occurrence rates are very large (~90%) at high and arctic latitudes and much smaller (~30–50%) at middle latitudes. This is in nice agreement with the occurrence rates of polar mesosphere summer echoes (PMSE) which are approximately 90% at ALOMAR and at Spitzbergen and much smaller at middle latitudes (Zecha and Röttger, 2009; Bremer et al., 2009; Latteck and Bremer, 2017). Note that PMSE rely on the presence of ice particles (amongst other parameters) whereby the size of these ice
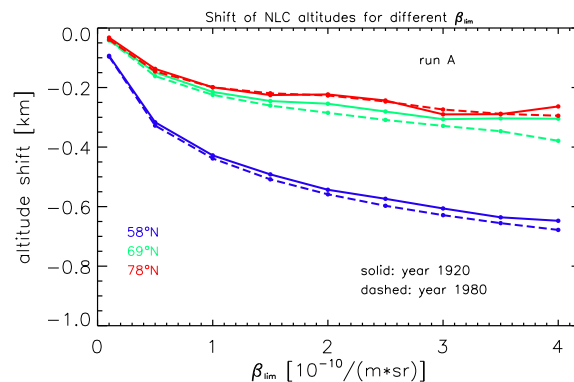

Fig. 7. (a) Geometric altitudes of β_{max} from run A (solid lines) and run C (dashed lines) applying a threshold of $\beta_{lim}=1$. Colors indicate different latitudes (see insert). (b) Altitudes from LIMA/MIMAS at 69°N for run A, B, and C (colors are explained in the insert). All yearly mean values of LIMA/MIMAS are shown (no averaging over half a solar cycle). Circles: Yearly mean NLC altitudes observed by the RMR lidar at ALOMAR (69°N) (update from Fiedler et al., 2017). The size of the bullets represents roughly the mean error of mean NLC altitudes. Inlay: expansion of the last years. Cross: mean NLC altitude with the mean of the standard deviations from all individual years. A threshold of $\beta_{lim}=4$ has been applied both to the model results and to the measurements.

Fig. 8. The change of NLC altitudes as a function of β_{lim} for run A and two years (1920, 1980) which are representative for the period before and after 1960, respectively. Changes are given with respect to the case $\beta_{lim}=0$. Colors indicate different latitudes (see insert).
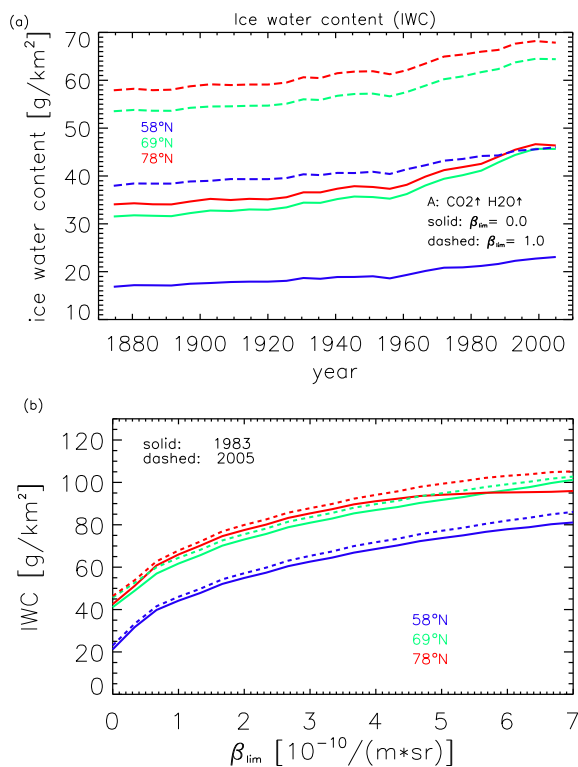
Fig. 9. (a) Ice water content (IWC) for run A applying thresholds of $\beta_{\lim}=0$ (solid lines) and $\beta_{\lim}=1$ (dashed lines). (b) IWC as a function of $\beta_{\lim}$ for two half solar cycle periods centered at 1983 and 2005, respectively. Colors indicate different latitudes (see insert).
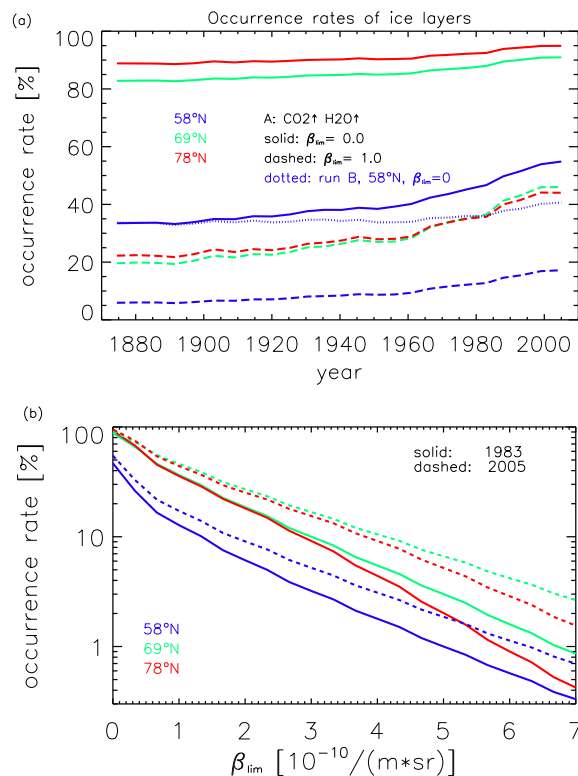

Fig. 10. Same as Fig. 9 but for occurrence rates. Results for run B are also shown in (a) but only for 58°N and $\beta_{\lim}=0$ (dotted line).

particles is less critical compared to NLC, i. e., even small ice particles can create PMSE (see Rapp and Lübken, 2003, for a review on PMSE).

When considering bins only where ice layers of significant magnitude are present ($\beta_{\lim}=1$, for example), occurrence rates are much smaller (Fig. 10a). At middle latitudes occurrence rates are only few percent because most latitude/longitude bins do not contain ice. Assuming that a spatial occurrence rate is equivalent to a temporal occurrence rate, this compares nicely with the occurrence rates of NLC observed by lidar at 54°N (Gerding et al., 2013). As can be seen from Fig. 10a and $\beta_{\lim}=0$, the increase of occurrence rates is significant at middle latitudes and much smaller at high/arctic latitudes where maximum saturation (100%) is approached. The dependence of occurrence rates on the choice of $\beta_{\lim}$ is shown in more detail in Fig. 10b. The occurrence rates are larger at high/polar latitudes (compared to middle latitudes) for all values of $\beta_{\lim}$ and drop exponentially with $\beta_{\lim}$ at all latitudes. The differences between the two periods shown in that Figure are due to the general trend.

5. Correlations and sensitivities

Many correlations can be studied involving ice layer parameters and background conditions. This concerns, for example, the relation between $\beta_{\max}$ and other ice layer parameters (radius, number densities, IWC, ice mass, etc.) but also the dependence on background conditions (temperatures at $\beta_{\max}$, water vapor concentrations at $\beta_{\max}$, or integrated H_2O where $S> 1$ etc.). These studies can be performed for all 3 runs and all 3 latitudes. Such a complete and systematic analysis of various dependencies is beyond the scope this paper and will be considered in the future. Here we concentrate on two important aspects, namely the dependence of NLC altitudes on CO_2 and CH_4 (relevant for trend studies), and the correlation between IWC and $\beta_{\max}$, relevant for the comparison between lidar and satellite observations. When studying the impact of CO_2 and H_2O we must realize that the temporal variations of

CO_2 and CH_4 (the precursor of H_2O) are rather similar. It is therefore important that runs where one or the other impact is fixed in time (runs B and C) are available. Furthermore, it is important to realize that we consider yearly mean values here. The results for correlations and sensitivities may be significantly different for individual events.

5.1. NLC altitude

The temporal change of CO_2 and NLC (geometric) altitudes at 69°N are very similar, as is highlighted in Fig. 11. This is true for run A and B (black and green lines), but not for run C (pink line). This stresses the fact that the decrease of NLC altitudes (z_{NLC}^{geo}) is mainly caused by shrinking of the atmosphere below that altitude, as discussed above. This strong similarity is also present at 58°N and 79°N (not shown) which implies that the shrinking argument applies at all latitudes.

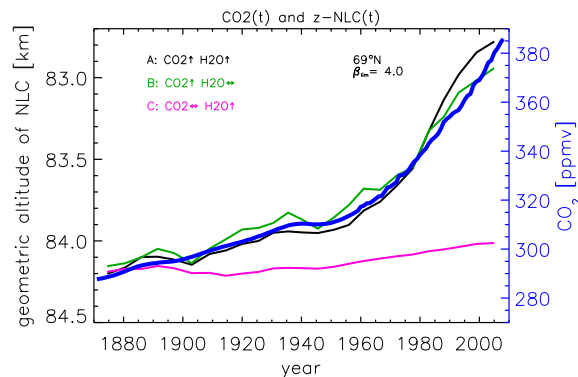Considering the similarity of the time series shown in Fig. 11 it is

Fig. 11. Time series of CO_2 (blue line, right axis) and geometric altitudes of NLC (left axis) for run A (black), run B (green), and run C (pink). Note the reversed altitude scale on the left axis.
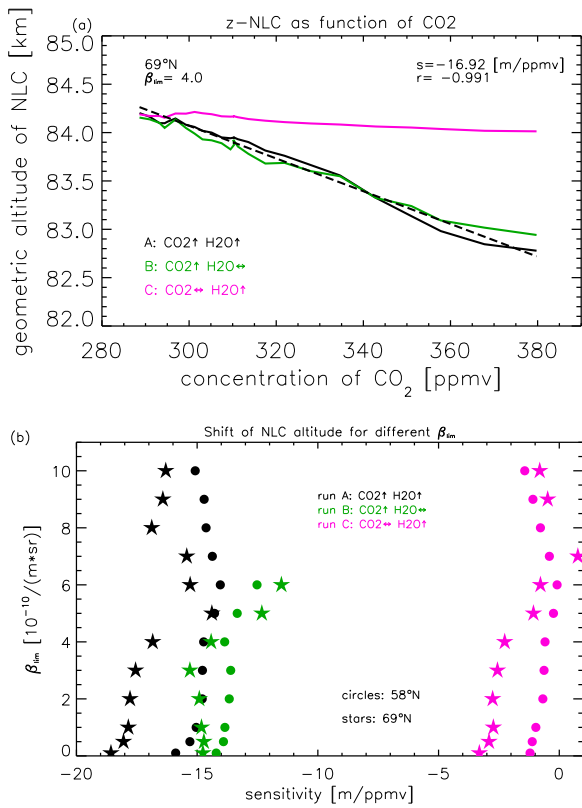
Fig. 12. (a) Geometric altitudes of NLC as a function of CO_2 concentration for runs A (black), B (green), and C (pink) and at 69°N applying a threshold of $\beta_{lim}=4$. Dashed line: linear fit to results from run A. The slope (s) and correlation coefficient (r) are given in the insert. (b) The sensitivity of NLC (geometric) altitudes to a change of CO_2 concentration as a function of β_{lim} for 58°N (circles) and 69°N (stars). Colors indicate different runs (see insert).

tempting to study the correlation between z_{NLC}^{geo} and CO_2 in more detail (Fig. 12a). Indeed, there is a strong anticorrelation (r~-0.98) between NLC (geometric) altitudes and CO_2. This is true for both runs where CO_2 increases (A, B), whereas the impact is negligible if only H_2O increases (run C). The straight line fit shown in Fig. 11 gives the sensitivity of NLC altitudes to changes of CO_2. This sensitivity is approximately s=−16.9 m/ppmv for run A at 69°N and for e.g. $\beta_{lim}=4$, and is slightly lower for run B (increase of CO_2 only). Does this sensitivity depend on the choice of β_{lim}? In Fig. 12b a systematic analysis of this sensitivity is shown as a function of β_{lim} and for middle and arctic latitudes (58°N, 69°N). For run A the sensitivity is on the order of −15 m/ppmv to −20 m/ppmv. An increase of CH_4 only (run C) also causes a slight decrease of z_{NLC}^{geo} which is, however, much smaller, namely −3 m/ppmv to 0 m/ppmv, depending on latitude and β_{lim}. The drop of NLC altitudes for increasing H_2O is caused by an enhanced accumulation of H_2O at NLC altitudes which allows somewhat larger temperatures (lower altitudes) to fulfill the S=1 condition (see above). If we consider a natural variability of yearly mean NLC altitudes of typically ±250 m (see Fig. 7) a sensitivity of −17 m/ppmv means that CO_2 would have to increase by ~250/17~15 ppmv so that a decrease of NLC altitudes would be detectable by observations.

5.2. Maximum backscatter and ice water concent

The ice water content is highly correlated to the maximum backscatter as can be seen in Fig. 13a for run A. The correlation coefficients and slopes for all latitudes and all runs are listed in Table 2 where all July mean data have been used (no smoothing over half a solar cycle). The correlation is similarly high for run C. Even for run B (increase of

Table 2
Correlations and sensitivities of July mean values 1871–2008.

latitude	run	slope	correlation
Ice water content[a] as function of β_{max}[b]			
58	A	11.52	0.983
58	B	11.19	0.865
58	C	10.18	0.986
69	A	13.15	0.988
69	B	16.11	0.891
69	C	15.45	0.993
78	A	14.12	0.984
78	B	18.93	0.875
78	C	16.95	0.991
Ice water content[a] as function of $H_2O@\beta_{max}$[c]			
58	A	4.66	0.918
58	B	2.77	0.294
58	C	5.07	0.984
69	A	8.86	0.933
69	B	1.22	0.063
69	C	11.61	0.997
78	A	8.38	0.932
78	B	4.16	0.176
78	C	12.46	0.997

All results for $\beta_{lim}=0$.
[a] Ice water content in g/km^2.
[b] β_{max} in $10^{-10}/(m\cdot sr)$.
[c] Water vapor in ppmv.

CO_2 only) the correlation is high, however, the variation of β_{max} is much smaller. The results are very similar for the other latitudes, namely 58°N and 78°N (see also Fig. 13a). The slopes of IWC (in g/km^2) as a function of β_{max} (in units of $10^{-10}/(m\cdot sr)$) depend on latitude, namely 11.5, 13.1,
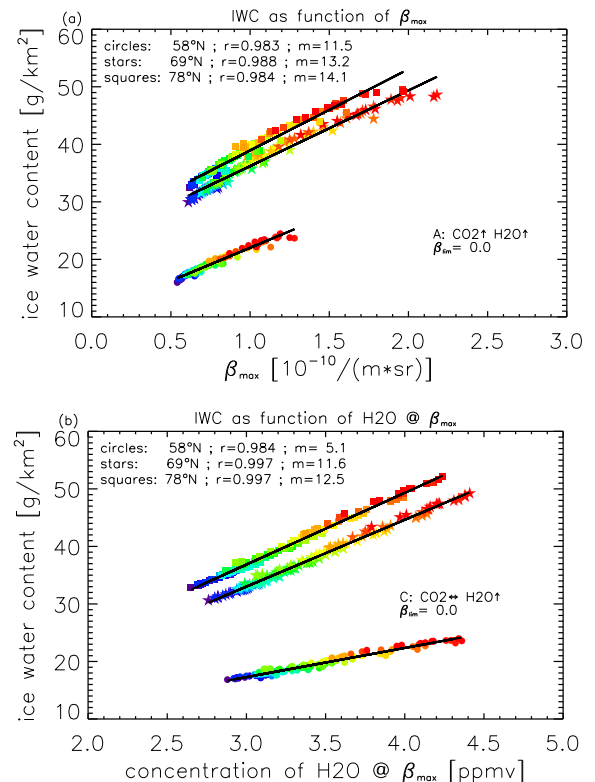

Fig. 13. (a) Ice water content (IWC) as a function of β_{max} for all years and run A. Colors indicate years from 1871 (blue) to 2008 (red). Symbols indicate latitude, namely 58°N (circles), 69°N (stars), and 78°N (squares). No threshold for β_{max} was applied ($\beta_{lim}=0$). Correlation coefficients (r) and slopes (m, in units given on the x/y-axis) are given in the insert. (b) Same but as a function of water vapor concentration at β_{max} and run C.

and 14.1 at 58°N, 69°N, and 78°N, respectively (all for run A). This implies that the increase of IWC with increasing β_{max} is stronger at higher latitudes. Furthermore, for a given β_{max}, IWC is larger at higher latitudes which is a consequence of ice particle radii and number densities (see section 4.3). The importance of this result is given by the opportunity to convert ground based lidar measurements of mean NLC brightness (β_{max}) to satellite borne observations of mean PMC (IWC), or vice versa. This offers the chance, for example, to compare precise local information with the morphology of ice layers on a more global scale, and to combine different data sets for long term trend analysis. We note that a correlation between IWC and albedo has been identified in satellite measurements, and that albedo is closely related to backscatter (Thomas et al., 2019).

The strong correlations shown in Fig. 13 lead to the assumption that both IWC and β_{max} are mainly determined by a common background ingredient, namely the concentration of water vapor. This idea is nicely confirmed when plotting IWC as a function of water vapor at β_{max} ($H_2O@\beta_{max}$, see Fig. 13b). The correlation is nearly perfect for run C at all latitudes, and still very high for run A (all latitudes), i. e., in both runs where H_2O increases, whereas the correlation is basically absent for run B (all latitudes), i. e., when H_2O is constant (not shown). Again, the correlation coefficients and slopes for all latitudes and all runs are listed in Table 2. The slopes of IWC as a function of $H_2O@\beta_{max}$ are similar at high and arctic latitudes (both for run A and C), but are significantly smaller at middle latitudes. This strong correlation allows to connect a measurement of mean backscatter from ice particles to an important background parameter, namely the mean concentration of water vapor at the altitude of β_{max}.

6. Further comparison with observations

Some comparisons have already been discussed in previous sections, for example regarding NLC altitudes at ALOMAR and Kühlungsborn, or the occurrence rates of PMSE. They all show excellent agreement within the limitations given by the observations (e.g., the length of the time series) and the model.

Phase height measurements of reflection heights are available since 1959. The reflection altitude of low frequency radio waves (162 kHz) in the ionosphere is measured which is given by a critical electron number density located close to NLC altitudes (descriptions of this method are available in Taubenheim et al., 1990; Peters et al., 2017, and references therein). The reflection altitude is closely related to a fixed pressure level which decreases with time according to the shrinking effect described above. A more recent analysis by Bremer and Peters (2008) shows that reflection heights decrease by ~30 m/dec in the period 1959 to 2006. This result is reproduced and compared to LIMA/MIMAS in Fig. 14a. Using LIMA/MIMAS results presented in this paper (run A, 58°N) and considering the same time period results in a drop of NLC (geometric) altitudes by −25 m/dec. This is in nice agreement with observations if we consider that radio reflection heights are also affected by other processes such as geomagnetic activity, solar cycle, and potential long term trends of nitric oxide. Furthermore, NLC altitudes deviate from a constant pressure level over time for reasons explained above. Our results confirm a more detailed comparison of trends from phase height measurements and LIMA published in Bremer and Berger (2002).

A study of the long term evolution of NLC brightness based on ground based visual observations was published by Pertsev et al. (2014). For the period 1990 to 2013 (24 years) they find a significant increase of brightness. However, when correcting for improvements of observational techniques and operations and taking into account the effect of solar cycle, they arrive at no significant increase of brightness in that period but even at a small decrease. Considering our LIMA/MIMAS results we expect an increase of β_{max} by approximately $0.10 \times 10^{-10}/(m\cdot sr)$ per decade with mean values of β_{max} ~2.7–4.5, depending on the choice of β_{lim} (1–4). This implies that the increase is roughly 2–4% per decade. This is much smaller than the relative uncertainty of the observational trend (~36%) which is

given by the error of the straight line fit (2.41 marks/dec) and the mean of 6.7 marks (see Fig. 2 in Pertsev et al., 2014). In other words, we cannot expect to detect a brightness change in the visual observations published by Pertsev et al. (2014) using the prediction from LIMA/MIMAS.

A summary of visual observations of NLC from Denmark and the UK in the period 1964–2006 was published by Kirkwood et al. (2008). This includes a trend study of the number of nights with NLC in the summer season (20 June–20 July, 31 days). Their results are reproduced in Fig. 14b for two cases, namely 'all NLC' and 'bright or very bright NLC' (nomenclature from that paper). A direct comparison of occurrence rates from LIMA/MIMAS and the number of NLC nights from visual observations is problematic for several reasons, e.g. impact of cloud cover, sensitivity of visual compared to lidar observations, spatial versus temporal variations, etc. We therefore decided to compare relative changes. In more detail we took the relative slopes of occurrence rates from LIMA/MIMAS for the period after 1960 (see Fig. 10a) for the cases $\beta_{lim}=0$ (corresponding to all NLC) and $\beta_{lim}=3$ (corresponding to bright or very bright NLC as in LBB18) and used these slopes to determine the expected trends of the number of nights (N_{LIMA}). The mean of N_{LIMA} was set to the mean of the observations. The results are shown in Fig. 14b (dashed lines). As can be seen the agreement is very good. We have used other values for β_{lim} (between 1 and 5) when deriving 'bright' clouds from LIMA/MIMAS. It turns out that the slope in Fig. 14b (blue dashed line) does not critically depend on the choice of β_{lim}. We repeat that this comparison primarily concerns the relative change with time and not the absolute values. We note, however, that for the selected β_{lim}-values (0 and 2, see above) the mean occurrence rates in the period 1960–2008
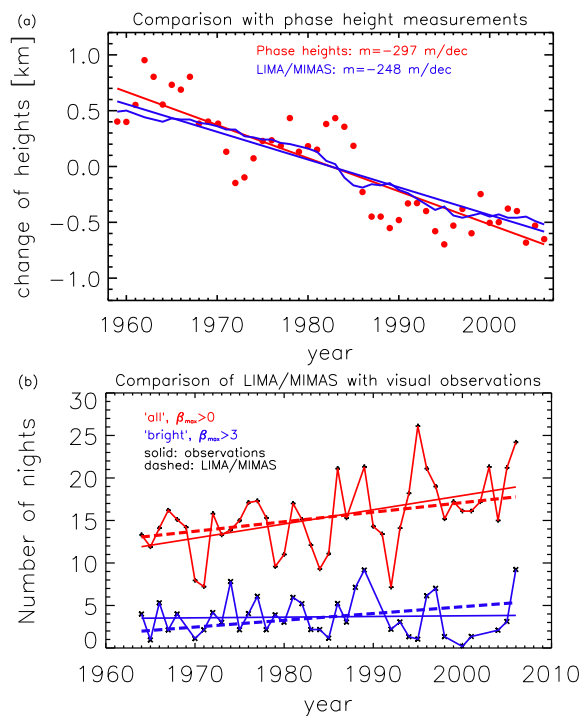

Fig. 14. (a) The change of radio wave reflection heights (red dots) and changes of geometric altitudes of NLC from LIMA/MIMAS (blue line). Mean values are set to zero in each case. Observational data points are from Bremer and Peters (2008). The slopes (m) of straight line fits (red and blue lines) are given in the insert. (b) The number of nights with observations of 'bright' (blue) and 'all' NLC (red) from Kirkwood et al. (2008) (points and solid lines). Occurrence rates from LIMA/MIMAS for $\beta_{lim}=3$ (dashed, blue) and $\beta_{lim}=0$ (dashed, red) are also shown. The means of LIMA/MIMAS data have been normalized to the observations (see text for more details).

are approximately 50% and 7% which corresponds closely to the mean number of days with NLC (~15.4 and 3.66) relative to the total number of days: 15.4/31≙49.7% and 3.66/31≙11%, respectively. We conclude that the long term development of nights with visual observations of NLC is consistent with the occurrence rate increase predicted by LIMA/MIMAS.

7. Discussion and conclusion

When comparing ice layer parameters, e.g., β_{max}, with local atmospheric background conditions it should be kept in mind that it can take several hours from nucleation of an ice particle to sublimation (Berger and von Zahn, 2002; Bardeen et al., 2010). During this time the particle has traveled a large horizonal distance and encountered a variety of ambient conditions. On the other hand, sophisticated microphysical modeling in the presence of small scale atmospheric variations has shown that the brightness of strong NLC depends mainly on background conditions encountered a few hours before observation (Kiliani et al., 2013). This implies that local atmospheric conditions are presumably representative for the morphology of (strong) NLC on scales of few hundred kilometers. Furthermore, we mainly study yearly mean values in this paper and have averaged over half a solar cycle. The variability within a year must be taken into account when judging the significance of trends or when comparing with observations. Some examples of distributions have been presented in sections 3 and 4. Note that each data point contributing to these distributions is an average of a huge number of individual ice particles.

The very first measurement of NLC heights in the late 19th century was published by Jesse (1896) and showed somewhat lower values (82.08 km) compared to the results published in this paper (83.8 km). We have discussed this difference in detail in LBB18. Note that a later summary of all nightly mean NLC heights in the period 1889–1891 by Gadsden and Schröder (1989) gave a median value of 82.9 km (mean: 83.6 km, standard deviation: 2.35 km). As is stated in that reference related to visual observations of NLC heights: *'The body of data is not sufficient to permit a discussion of trends'*. In summary, the observational data base is rather limited and the variability in LIMA/MIMAS ($\pm$0.6 km, 2σ-value) as well as the natural variability known from precise lidar measurements need to be taken into account (the mean of standard deviations from lidar observations is $\Delta z=\pm 1.1$ km). Furthermore, systematic effects need to be considered such as the impact of presumably high H_2O concentrations (caused by the eruption of Krakatau) on z_{NLC}^{geo}, and a systematic bias of ground based visual observations towards too low heights compared to z_{NLC}^{geo} (Ridder et al., 2017). In summary, we do not consider the difference between the observations of NLC heights by Jesse (1896) and our model to be problematic.

We note that very bright NLC of roughly $\beta_{max} >10$ are missing at high and arctic latitudes in LIMA/MIMAS. Such strong NLC are occasionally observed by the RMR lidar at ALOMAR, however, only for short periods, i. e., smaller than the minimum time slot in the model output of 6 h. Apart from this, the lack of very bright NLC in the model could be due to the absence of variations caused by gravity waves which (if of appropriate magnitude and period) can cause a significant brightness enhancement (Rapp et al., 2002; Kiliani et al., 2013). We note that also tides play a substantial role in causing local enhancements of NLC brightness (Stevens et al., 2010; Schmidt et al., 2018). We consider it likely that these effects do not impact the main conclusions of this paper.

We note that climate change most likely affects the general circulation, e. g., the Brewer-Dobson circulation (BDC), which might lead to secondary effects such as composition changes in the stratosphere or modification of gravity wave sources, propagation, and dissipation (see, for example, Butchart, 2014). Unfortunately, very little is known on the long term effects of these changes on the dynamical, thermal, and compositorial structure of the summer mesopause region. We therefore decided not to speculate on such effects and keep background winds and

gravity wave forcing constant. On the other hand, model results on climate change effects on the circulation in the middle atmosphere (including gravity wave forcing and water vapor transport) can presumably be tested against the observed persistency of some of the NLC parameters discussed in this paper.

This study concentrates on trends of ice layer parameters and background conditions on decadal timescales. It is well known that several processes potentially affect NLC on shorter time scales, for example, solar cycle, ozone recovery, gravity waves and planetary waves, volcanoes, and the transport of water paper from below. These effects are not considered in this paper and will be subject of future studies.

In summary, we have presented trends derived from a background (LIMA) and an ice particle model (MIMAS) for a period of 138 years. We have performed model runs with and without an increase of CO_2 and H_2O. Most parameters show significant trends, mainly after approximately 1960 when the enhancement of both CO_2 and H_2O accelerates. For some parameters it is important to distinguish between geometric and pressure altitudes. For example, the geometric altitude of NLC decreases by approximately 1.5 km in 138 years, nearly independent of latitude and mainly after 1960. This decrease is to a large extent caused by shrinking of the entire middle atmosphere below NLC heights. Trends of NLC altitudes (and temperatures) on pressure levels are much smaller. Several ice layer and background parameters are similar at high (69°N) and arctic (78°N) latitudes, but deviate substantially at mid-latitudes (58°N). This concerns, for example, occurrence rates, ice water content, and number of ice particles. It is therefore plausible that experimental and/or model studies of mesospheric ice layers at, for example, ALOMAR (69°N) are representative for the entire northern hemisphere polar cap. NLC at middle latitudes occur preferentially in regions where temperatures are lower compared to other locations in the same latitude band. At high and arctic latitudes ice particles are present nearly everywhere.

Considering the time period after 1960, geometric altitudes of NLC decrease by approximately 260 m per decade, and brightness increases by roughly 50%, independent of latitude. Roughly speaking, increases of NLC brightness and ice particle radii are caused by an enhancement of water vapor concentration, whereas trends of (geometric) NLC altitudes are due to cooling caused by an increase of CO_2. NLC altitudes decrease by approximately 15–20 m per increase of CO_2 by 1 ppmv. The number of ice particles in a column and also at an altitude of β_{max} is nearly constant with time. At all latitudes, yearly mean NLC appear at altitudes where temperatures are close to 145$\pm$1 K. In the main summer season (here: July) ice particles are present nearly all the time at high and arctic latitudes, whereas the occurrence rate is much smaller at middle latitudes. We find a strong correlation between yearly mean ice water content (IWC) and maximum backscatter (β_{max}), where the slope depends on latitude. This allows to combine data sets from satellites and lidars for, e.g., long term studies. Note that nearly all results regarding trends (including their latitudinal dependence) depend on β_{lim}, i. e., on the lower limit applied for β_{max}. Prominent examples are occurrence rates and ice water content.

We compared our simulations with observations, including visual observations and NLC measurements by lidar as well es radar backscattering which is indirectly linked to ice particles. The parameters derived from these observations, e.g., trends of nights with NLC (visual), altitude of maximum backscatter (lidar), and occurrence frequencies (radar) are all in very good agreement with our model results. In general, limitations given by the observations (e.g., measurement precision or the length of the time series) and the model (see above) need to be taken into account when trying to detect trends.

Declaration of competing interest

The authors declare that they have no known competing financial interests or personal relationships that could have appeared to influence

the work reported in this paper.

Acknowledgements

We thank Jens Fieder for providing an update of the lidar data from ALOMAR. We acknowledge the Mauna Loa records for CO_2 and CH_4 from http://www.esrl.noaa.gov/gmd/ccgg/. This paper is partly supported by the TIMA project of the BMBF research initiative ROMIC and by the PACOG project of the German Research Foundation (DFG).

References

Bardeen, C.G., Toon, O.B., Jensen, E.J., Hervig, M.E., Randall, C.E., Benze, S., Marsh, D. R., Merkel, A., 2010. Numerical simulations of the three-dimensional distribution of polar mesospheric clouds and comparisons with Cloud Imaging and Particle size (CIPS) experiment and the Solar Occultation for Ice Experiment (SOFIE) observations. J. Geophys. Res. 115.

Baumgarten, G., Lübken, F.-J., Fricke, K., 2002. First observation of one noctilucent cloud by a twin lidar in two different directions. Ann. Geophys. 20, 1863–1868.

Berger, U., 2008. Modeling of middle atmosphere dynamics with LIMA. J. Atmos. Sol. Terr. Phys. 70, 1170–1200.

Berger, U., Baumgarten, G., Fiedler, J., Lübken, F.-J., 2019. A new description of probability density distributions of Polar Mesospheric Clouds. Atmos. Chem. Phys. 19, 4685–4702.

Berger, U., Lübken, F.-J., 2011. Mesospheric temperature trends at mid-latitudes in summer. Geophys. Res. Lett. 38.

Berger, U., Lübken, F.-J., 2015. Trends in mesospheric ice layers in the Northern Hemisphere during 1961 - 2013. J. Geophys. Res. 120, 11,277–11,298.

Berger, U., von Zahn, U., 2002. Icy particles in the summer mesopause region: tree-dimensional modeling of their environment and two-dimensional modeling of their transport. J. Geophys. Res. 107 (A11) https://doi.org/10.1029/2001JA000316.

Bremer, J., Berger, U., 2002. Mesospheric temperature trends derived from ground-based LF phase-hight observations at mid-latitudes: comparison with model simulations. J. Atmos. Sol. Terr. Phys. 64, 805–816.

Bremer, J., Hoffmann, P., Latteck, R., Singer, W., Zecha, M., 2009. Long-term changes of (polar) mesosphere summer echoes. J. Atmos. Sol. Terr. Phys. 1571–1576.

Bremer, J., Peters, D., 2008. Influence of stratospheric ozone changes on long-term trends in the meso- and lower thermosphere. J. Atmos. Sol. Terr. Phys. 70, 1473–1481.

Butchart, N., 2014. The Brewer-Dobson circulation. Rev. Geophys. 52, 157–184.

Chu, X., Gardner, C., Roble, R., 2003. Lidar studies of interannual, seasonal and diurnal variations of polar mesospheric clouds at the South pole. J. Geophys. Res. 108 (No. D8), 8447. https://doi.org/10.1029/2002JD002524.

Collins, R.L., Taylor, M.J., Nielsen, K., Mizutani, K., Murayama, Y., Sakanoi, K., DeLand, M.T., 2009. Noctilucent cloud in the western Arctic in 2005: simultaneous lidar and camera observations and analysis. J. Atmos. Sol. Terr. Phys. 446–452.

Compo, G.P., Whitaker, J.S., Sardeshmukh, P.D., Matsui, N., Allan, R.J., X Yin, B.E., Gleason, J., Vose, R.S., Rutledge, G., Bessemoulin, P., Brönnimann, S., Brunet, M., Crouthamel, R.I., Grant, A.N., Groisman, P.Y., Jones, P.D., Kruk, M.C., Kruger, A.C., Marshall, G.J., Maugeri, M., Mok, H.Y., Nordli, Ø., Ross, T.F., Trigo, R.M., Wang, X. L., Woodruff, S.D., Worley, S.J., 2011. The twentieth century reanalysis project. Quart. J. R. Met. Soc. 137, 1–28.

DeLand, M.T., Thomas, G.E., 2015. Update PMC trends derived from SBUV data. J. Geophys. Res. 120, 2140–2166.

Eidhammer, T., Havnes, O., 2001. Size dependence of the mesospheric dust temperature and its influence on the noctilucent clouds and polar mesosphere summer echo phenomena. J. Geophys. Res. 106, 24831–24841.

Espy, P.J., Jutt, H., 2002. Equilibrium temperature of water-ice aerosols in the high-latitude summer mesosphere. J. Atmos. Sol. Terr. Phys. 64, 1823–1832.

Etheridge, D., Steele, L., Langenfelds, R., Francey, R., Barnola, J.-M., Morgan, V., 1998. Historical CO_2 Records from the Law Dome DE08, DE08-2, and DSS Ice Cores. Carbon Dioxide Information Analysis Center. Oak Ridge National Laboratory, U.S. Department of Energy, Oak Ridge, Tenn., U.S.A.

Fiedler, J., Baumgarten, G., Berger, U., Lübken, F.-J., 2017. Long-term variations of noctilucent clouds at ALOMAR. J. Atmos. Sol. Terr. Phys. 162, 79–89.

Gadsden, M., Schröder, W., 1989. Noctilucent Clouds. Springer-Verlag, New York.

Garcia, R.R., Marsh, D.R., Kinnson, D.E., Boville, B.A., Sassi, F., 2007. Simulation of secular trends in the middle atmosphere, 1950-2003. J. Geophys. Res. 112 (D09301).

Gerding, M., Höffner, J., Hoffmann, P., Kopp, M., Lübken, F.-J., 2013. Noctilucent cloud variability and mean parameters from 15 years of lidar observations at a mid-latitude site (54°N, 12°E). J. Geophys. Res. 118, 317–328.

Gerding, M., Höffner, J., Rauthe, M., Singer, W., Zecha, M., Lübken, F.-J., 2007. Simultaneous observation of noctilucent clouds, mesospheric summer echoes, and temperature at a midlatitude station (54°N). J. Geophys. Res. 112.

Gerrard, A.J., Kane, T.J., Thayer, J.P., 1998. Noctilucent clouds and wave dynamics: observations at Sondrestrom, Greenland. Geophys. Res. Lett. 25, 2817–2820.

Hansen, G., Serwazi, M., von Zahn, U., 1989. First detection of a noctilucent cloud by lidar. Geophys. Res. Lett. 16, 1445–1448.

Hervig, M.E., Berger, U., Siskind, D.E., 2016a. Decadal variability in PMCs and implications for changing temperature and water vapor in the upper mesosphere. J. Geophys. Res. 121, 2383–2392.

Hervig, M.E., Gerding, M., Stevens, M.H., Stockwell, R., Bailey, S.M., Russell III, J.M., Stober, G., 2016b. Mid-latitude mesospheric clouds and their environment from SOFIE observations. J. Atmos. Sol. Terr. Phys. 149, 1–14.

Hervig, M.E., Siskind, D.E., Bailey, S.M., Russell III, J.M., 2015. The influence of PMCs on water vapor and drivers behind PMC variability from SOFIE observations. J. Atmos. Sol. Terr. Phys. 132, 124–134.

Jesse, O., 1896. Die Höhe der leuchtenden Nachtwolken. Astron. Nachr. 140, 161–168.

Kiliani, J., Baumgarten, G., Lübken, F.-J., Berger, U., Hoffmann, P., 2013. Temporal and spatial characteristics of the formation of strong noctilucent clouds. J. Atmos. Sol. Terr. Phys. 104, 151–166.

Kirkwood, S., Dalin, P., Réchou, A., 2008. Noctilucent clouds observed from the UK and Denmark - trends and variations over 43 years. Ann. Geophys. 26, 1243–1254.

Latteck, R., Bremer, J., 2017. Long-term variations of polar mesospheric summer echoes observed at Andøya 69°N. J. Atmos. Sol. Terr. Phys. 163, 31–37.

Lübken, F.-J., Berger, U., Baumgarten, G., 2009. Stratospheric and solar cycle effects on long-term variability of mesospheric ice clouds. J. Geophys. Res. 114.

Lübken, F.-J., Berger, U., Baumgarten, G., 2013. Temperature trends in the midlatitude summer mesosphere. J. Geophys. Res. 118, 13347–13360.

Lübken, F.-J., Berger, U., Baumgarten, G., 2018. On the anthropogenic impact on long-term evolution of noctilucent clouds. Geophys. Res. Lett. 45, 6681–6689.

Lübken, F.-J., Fricke, K.-H., Langer, M., 1996. Noctilucent clouds and the thermal structure near the Arctic mesopause. J. Geophys. Res. 101, 9489–9508.

Marsh, D.R., Mills, M.J., Kinnison, D.E., Lamarque, J.-F., Calvo, N., Polvani, L.M., 2013. Climate change from 1850 to 2005 simulated in CESM1(WACCM). J. Clim. 26, 7372–7390.

Medvedev, A.S., Klaassen, G.P., 2000. Parameterization of gravity wave momentum deposition based on nonlinear wave interactions: basic formulation and sensitivity tests. J. Atmos. Sol. Terr. Phys. 62, 1015–1033.

Olivero, J.J., Thomas, G.E., 1986. Climatology of polar mesospheric clouds. J. Atmos. Sci. 43, 1263–1274.

Pertsev, N., Dalin, P., Perminov, V., Romejko, V., Dubietis, A., Balčiunas, R., Černis, K., Zalcik, M., 2014. Noctilucent clouds observed from the ground: sensitivity to mesospheric parameters and long-term time series. Earth Planets Space 66 (98).

Peters, D.H.W., Entzian, G., Keckhut, P., 2017. Mesospheric temperature trends derived from standard phase-height measurements. J. Atmos. Sol. Terr. Phys. 163, 23–30.

Rapp, M., Lübken, F.-J., 2003. On the nature of PMSE: electron diffusion in the vicinity of charged particles revisited. J. Geophys. Res. 108 (D8), 8437. https://doi.org/10.1029/2002JD002857.

Rapp, M., Lübken, F.-J., Müllemann, A., Thomas, G., Jensen, E., 2002. Small scale temperature variations in the vicinity of NLC: experimental and model results. J. Geophys. Res. 107 (D19).

Rapp, M., Thomas, G.E., 2006. Modeling the microphysics of mesospheric ice particles: assessment of current capabilities and basic sensitivities. J. Atmos. Sol. Terr. Phys. 68, 715–744.

Ridder, C., Baumgarten, G., Fiedler, J., Lübken, F.-J., Stober, G., 2017. Analysis of small-scale structures in lidar observations of noctilucent clouds. J. Atmos. Sol. Terr. Phys. 162, 48–56.

Roble, R.G., Dickinson, R.E., 1989. How will changes in carbon dioxide and methane modify the mean structure of the mesosphere and thermosphere? Geophys. Res. Lett. 16, 1441–1444.

Russell III, J.M., Rong, P., Hervig, M.E., Siskind, D.E., Stevens, M.H., Bailey, S.M., Gumbel, J., 2015. Analysis of northern midlatitude noctilucent cloud occurrences using satellite data and modeling. J. Geophys. Res. 119, 3238–3250.

Schmidt, F., Baumgarten, G., Berger, U., Fiedler, J., Lübken, F.-J., 2018. Local time dependence of polar mesospheric clouds: a model study. Atmos. Chem. Phys. 18, 8893–8908.

Shettle, E.P., Thomas, G.E., Olivero, J.J., Evans, W.F.J., Debrestian, D.J., Chardon, L., 2002. Three-satellite comparison of polar mesospheric clouds: evidence for long-term change. J. Geophys. Res. 107 (D12), 4134. https://doi.org/10.1029/2001JD000668.

Stevens, M.H., Siskind, D.E., Eckermann, S.D., Coy, L., McCormack, J.P., Englert, C.R., Hoppel, K.W., Nielsen, K., Kochenash, A.J., Hervig, M.E., Randall, C.E., Lumpe, J., Bailey, S.M., Rapp, M., Hoffmann, P., 2010. Tidally induced variations of polar mesospheric cloud altitudes and ice water content using a data assimilation system. J. Geophys. Res. 115.

Taubenheim, J., von Cossart, G., Entzian, G., 1990. Evidence of CO2-induced progressive cooling of the middle atmosphere derived from radio observations. Adv. Space Res. 10 (10), 171–174.

Thomas, G., 1996. Is the polar mesosphere the miner's canary of global change? Adv. Space Res. 18 (3), 149–158.

Thomas, G., Lumpe, J., Bardeen, C., Randall, C., 2019. Albedo-cce regression method for determining ice water content of polar mesospheric clouds using ultraviolet observations from space. Atmos. Meas. Tech. 12, 1755–1766.

Thomas, G., Olivero, J., DeLand, M., Shettle, E., 2003. Comment on 'are noctilucent clouds truly a 'miner's canary' for global change? EOS 84 (36), 352–353.

Thomas, G.E., Olivero, J.J., Jensen, E.J., Schröder, W., Toon, O.B., 1989. Relation between increasing methane and the presence of ice clouds at the mesopause. Nature 338, 490–492.

von Cossart, G., Fiedler, J., von Zahn, U., 1999. Size distributions of NLC particles as determined from 3-color observations of NLC by ground-based lidar. Geophys. Res. Lett. 26, 1513–1516.

von Zahn, U., 2003. Are noctilucent clouds truly a 'miner's canary' for global change? EOS 84 (28), 261–264.

von Zahn, U., Berger, U., 2003. Persistent ice cloud in the midsummer upper mesosphere at high latitudes: three-dimensional modeling and cloud interactions with ambient water vapor. J. Geophys. Res. 108 (D8), 8451. https://doi.org/10.1029/2002JD002409.

von Zahn, U., von Cossart, G., Fiedler, J., Rees, D., 1998. Tidal variations of noctilucent clouds measured at 69° latitude by groundbased lidar. Geophys. Res. Lett. 25, 1289–1292.

Zecha, M., Röttger, J., 2009. Occurrence of polar mesosphere summer echoes at very high latitudes. Ann. Geophys. 27 (3), 1331–1342.